# Matrix-Pencil Approach-Based Interference Mitigation for FMCW Radar Systems

Wang, Jianping; Ding, Min; Yarovoy, Alexander

**DOI**
10.1109/TMTT.2021.3090798

**Publication date**
2021

**Document Version**
Final published version

**Published in**
IEEE Transactions on Microwave Theory and Techniques

# Matrix-Pencil Approach-Based Interference Mitigation for FMCW Radar Systems

Jianping Wang, *Member, IEEE*, Min Ding, and Alexander Yarovoy, *Fellow, IEEE*

***Abstract*— A novel matrix-pencil (MP)-based interference mitigation approach for frequency-modulated continuous-wave (FMCW) radars is proposed in this article. The interference-contaminated segment of the beat signal is first cut out, and then, the signal samples in the cutout region are reconstructed by modeling the beat signal as a sum of complex exponentials and using the MP method to estimate their parameters. The efficiency of the proposed approach for the interference with different parameters (i.e., interference duration, signal-to-noise ratio (SNR), and different target scenarios) is investigated by means of numerical simulations. The proposed interference mitigation approach is intensively verified on experimental data. Comparisons of the proposed approach with the zeroing and other beat-frequency interpolation techniques are presented. The results indicate the broad applicability and superiority of the proposed approach, especially in low SNR and long interference duration situations.**

***Index Terms*— Frequency-modulated continuous-wave (FMCW) radar, interference mitigation, matrix pencil, signal fusion.**

## I. Introduction

FREQUENCY-MODULATED continuous-wave (FMCW) radars are widely used in both civilian and military applications due to their simple processing method, high accuracy, and high reliability. With the explosive increase in wireless radio and sensing applications, FMCW radars face increasingly severe interference from other devices. For instance, modern cars are equipped with multiple FMCW radars to assist drivers and improve transportation safety, where the radars inevitably cause strong interference among each other. Moreover, FMCW weather radars also suffer from radio frequency interference from the surrounding environment. In these situations, the strong interference leads to reduced radar sensitivity and resolution, weak target masking, and probably ghost target detection. Therefore, to overcome these problems and alleviate performance degradation of the radar systems, it is crucial to take proper interference mitigation in practice.

So far, a number of approaches have been proposed for interference migration, which can be mainly classified into two categories: 1) system-level approaches and 2) postsignal processing techniques. System-level approaches exploit temporal, spatial, polarization, frequency, and code diversities in the radar system, the antenna array, and the waveform design. In [1], a circular polarized antenna architecture is design to combat the linear polarized interference. Meanwhile, the frequency hopping technique learned from bats is also generally used to counteract various interference caused by spectrum congestion [2]. In [3], the slopes of FMCW sweeps are devised to change in a predefined pattern and hundreds of sweeps form a burst; then, the beat signals of targets within a burst form a specific pattern in the spectrogram, which makes them distinct from interference patterns caused by aggressor radars. The medium access control (MAC)-like approach is proposed to regulate transmission time of the multiple radars in the same area [4], [5]. These approaches provide an effective solution to interference mitigation, but they increase the complexity of radar systems or antenna designs for implementation and lead to costly systems.

On the other hand, the postsignal processing techniques utilize a range of digital signal processing approaches to mitigate interference probably at the expense of increased computational load. The signal processing methods can be further divided into three classes: filtering approaches [6], [7], signals separation [8], [9], and suppression and reconstruction approaches [10]–[13]. In [6], weighted-envelope normalization approaches are proposed to deal with strong spiky mutual interference by detecting the envelope variations within a sliding time window and inversely normalizing the detected interference. In [7], an adaptive noise canceller is devised for mutual interference suppression by exploiting the different distributions of frequency spectra of target's signals and mutual interference in the frequency domain. However, both filtering approaches are only applicable to tackle certain types of interference or point-like targets scenario, which limits their wide applications. Meanwhile, the stability of the adaptive filter is hard to guarantee.

The signals' separation methods generally exploit different features, i.e., distinct sparsity of targets' signals and the interference in different transform domains to separate them [8], [9]. Thus, these methods require some prior information about the sparsity of the desired signal and the related

Manuscript received February 21, 2021; revised May 5, 2021 and June 9, 2021; accepted June 12, 2021. *(Corresponding author: Jianping Wang.)*

This work did not involve human subjects or animals in its research.

Jianping Wang and Alexander Yarovoy are with the Faculty of Electrical Engineering, Mathematics and Computer Science (EEMCS), Delft University of Technology, 2628 CD Delft, The Netherlands (e-mail: j.wang-4@tudelft.nl; a.yarovoy@tudelft.nl).

Min Ding was with the Faculty of Electrical Engineering, Mathematics and Computer Science (EEMCS), Delft University of Technology, 2628 CD Delft, The Netherlands. She is now with State Grid Corporation of China, Beijing 100031, China (e-mail: min.dingchina@hotmail.com).

Color versions of one or more figures in this article are available at https://doi.org/10.1109/TMTT.2021.3090798.

Digital Object Identifier 10.1109/TMTT.2021.3090798

interference to construct proper bases for optimal separation. However, if the "off-grid" problem between the bases (e.g., the discrete Fourier basis and short-time Fourier transform basis [8]) and the signal to be represented exists, it would lead to some loss of the degree of sparsity, thus degrading the separation performance.

By contrast, as long as the extension of the interference is limited in a certain domain, the simplest but effective method to suppress the interference is, in practice, to directly cut the interference-contaminated samples out of the signal with various windows (e.g., zeroing and inverse cosine window) [14], [15]. However, the interference cutting-out not just eliminates the interference but also suppresses part of the useful signal of targets, which reduces the signal-to-noise ratio (SNR) of the targets after coherent processing and decreases the range resolution. To deal with the SNR loss problem, a Burg method-based interpolation was used to extrapolate the useful signal samples in the cutout region in the time–frequency ($t$–$f$) domain [11]. It separately uses the signal samples in the front and back of the cutout gap to extrapolate the cutout data forward and backward based on the related estimated autoregressive (AR) models. Then, the forward- and backward-extrapolated samples in the cutout region are summed up with weights by a specifically designed cross-fading window. This method is generally applicable to mitigate various interference for FMCW radars (as indicated in Fig. 2). However, its extrapolation accuracy degrades dramatically when the number of cutout samples of signals increases. In [12], the signal extrapolation with the AR model was suggested using the instrumental variable method (IVM). However, this method is not very stable and cannot always get proper signal reconstruction. In [13], instead of using parametric models, an iterative method with adaptive thresholding (IMAT) was used to recover the signal samples in the cutout region by exploiting the possible spectral sparsity of targets' beat signals. By using the fast Fourier transform (FFT) algorithm in implementation, this method could be very efficient. However, its reconstructed samples could have a large phase difference from the ground truth, which would significantly affect following phase-based signal processing, for instance, direction-of-arrival (DOA) estimation and polarimetric decomposition.

To accurately extrapolate the cutout data after cutout operation (i.e., zeroing), we propose an iterative matrix-pencil (MP) method-based extrapolation for interference mitigation. Similar to the Burg method-based approach, the proposed approach first cuts the interference-contaminated samples out of the signals and then reconstructs/extrapolates the clipped samples of the useful signals. However, the proposed approach simultaneously accounts for the signals before and after the clipped samples by using a unified all-pole model, which is derived from the analytical model of the beat signals of targets. Thus, it provides the potential to get a more accurate extrapolation of the noncontaminated signal in the cutout region. Before the extrapolation, the all-pole model is first estimated based on the interference-free samples with the MP method [16], [17]. However, in practice, the noise and the possible discontinuity of the interference-free samples would impact the accuracy of the estimated signal model, thus resulting in less accurate reconstruction of the cutout samples of useful signals. To alleviate this effect, an iterative scheme is introduced to refine the model estimation and the extrapolation, which significantly improves the accuracy of the signals in the cutout region. Moreover, we want to mention that a method similar to the one presented in this article has been used for multiband signal fusion for high-resolution imaging in [18] and [19]. In fact, for interference mitigation, the measured signals become two or more separate segments after interference suppression. Thus, using the interference-free signal segments to reconstruct/extrapolate the cutout region is in essence a signal fusion problem. The main difference is the absence of the incoherence correction between different signal segments needed for interference mitigation. Note this article focuses on interference mitigation on sweeps in the time domain, which would be flexible to be followed by other further processing. Nevertheless, we should mention that, in the case of interference mitigation followed by some specific 2-D processing (e.g., range-Doppler (R-D) processing and range-DOA estimation), the proposed interference mitigation approach could also be extended and implemented in the high-dimensional space by exploiting the 2-D or high-dimensional MP approaches [20], [21], which would be considered in future.

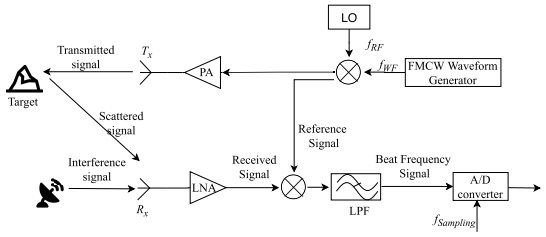


Fig. 1. General block diagram of the monostatic linear FMCW radar system.

The rest of this article is organized as follows. Section II formulates the basic models of the signals received by FMCW radars. In Section III, the proposed iterative MP method-based interference mitigation approach is presented. Then, its performance of interference mitigation is demonstrated in different scenarios through the numerical simulations in Section IV and the experimental results in Section V. Finally, conclusions are drawn in Section VI.

## II. FMCW Radar System Model

### A. Transmitted and Received Signals

The system diagram of an FMCW radar system is shown in Fig. 1. The transmitted FMCW signal can be expressed as

$$p(t) = A_{tx} \exp\left[ j2\pi \left( f_0 + \frac{1}{2} K t \right) t \right] \tag{1}$$

for $0 < t < T$, where $A_{tx}$ is the amplitude of the transmitted signal, and $f_0$ is the starting frequency of an FMCW sweep. $K = B/T$ is the chirp rate defined by the ratio of the signal bandwidth $B$ and the sweep time $T$. The transmitted electromagnetic (EM) signal is intercepted by targets and scattered back to the receiver. Considering the quasi-monostatic configuration of the transmit and receive antennas and assuming

single-scattering process for each target, the backscattered signal can be represented as

$$s_r(t) = \sum_{i=1}^{M} A_{rx,i} \exp\left[ j2\pi \left( f_0(t - t_i) + \frac{K}{2}(t - t_i)^2 \right) \right] \quad (2)$$

where $t_i = 2d_i/c$ is round-trip time delay of the scattered signal related to the $i$th target at a distance of $d_i$, and $A_{rx,i}$ is the corresponding amplitude of the signal, which subsumes the scattering coefficient and the propagation loss. $c$ is the speed of light, and $M$ is the number of targets.

### *B. Dechirp on Receiver*

In the FMCW radar system, dechirp processing is commonly used due to its simple operation and low requirement of sampling rate for the analog-to-digital converter (ADC). It is implemented by mixing the received signals with the conjugate of the transmitted one, which leads to beat signals.

Considering the occurrence of strong interference $s_{\text{int}}$, the beat signal after demodulating and filtering can be formulated in (3), as shown at the bottom of the page, where the superscript $^*$ denotes the complex conjugate and $\mathcal{F}_{lp}$ is the low-pass filter operator. $\tilde{A}_{r,i}$ is the amplitude of the received signal of the $i$th target, and $M'(\leq M)$ is the number of observed scatterers within the desired unambiguous range. As $\exp[-j2\pi(f_0\ t_i - ((Kt_i^2)/2))]$ is a constant phase term related to the $i$th target, which can be subsumed by the amplitude of the signal, one can present $a_i = \tilde{A}_{r,i} \exp[-j2\pi(f_0\ t_i - ((Kt_i^2)/2))]$ as a new complex signal amplitude. Then, (3) can be rewritten as a sum of complex exponential functions

$$\tilde{s}(t) = \mathcal{F}_{lp}\left(s_{\text{int}}(t) \cdot p^*(t)\ \right) + \sum_{i=1}^{M'} a_i \exp\left(-j2\pi f_{b,i} t\right) \quad (4)$$

where $f_{b,i} = Kt_i$ is the beat frequency corresponding to the $i$th target. For moving targets, $t_i = 2d_i/c = 2(d_{i0} + v_i t)/c$ can be used to account for the Doppler shift, where $v_i$ and $d_{i0}$ are the velocity and the initial distance of the $i$th target relative to the radar. Generally, as $v_i \ll c$, it has negligible impact on the target's beat frequency within a short FMCW sweep. After getting beat frequencies, the ranges of different targets can be calculated as

$$d_i = \frac{c \cdot f_{b,i}}{2K}. \quad (5)$$

As thermal noise and measurement errors always exist due to physical limitation of the practical radar system, the signal

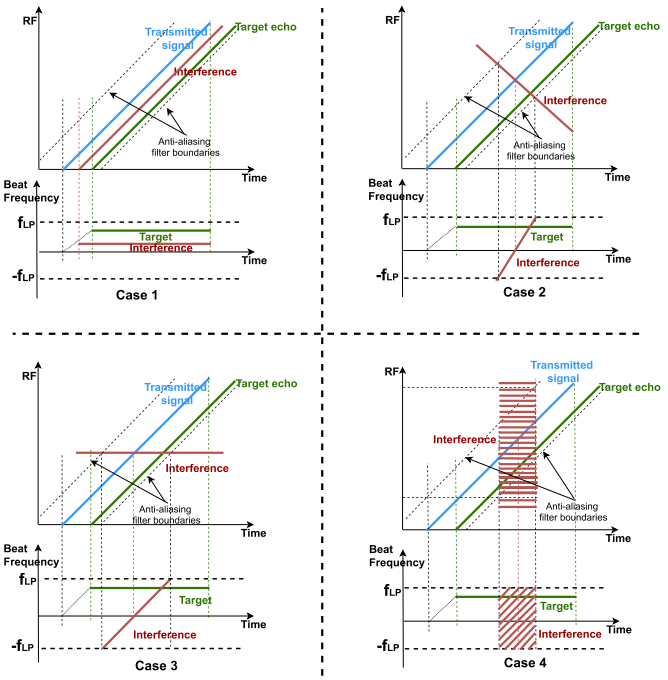


Fig. 2. Four cases of interference which corrupt the FMCW radar system. Case 1: chirp interference with the identical sweep parameters as the victim radar. Case 2: chirp interference with different sweep parameters from the victim radar. Case 3: sinusoidal/narrowband continuous interference. Case 4: instantaneous wideband interference.

measurements can be modeled as

$$\begin{aligned} s(t) &= \tilde{s}(t) + n(t) \\ &= \sum_{i=1}^{M'} a_i \exp(-j2\pi f_{b,i} t) + \mathcal{F}_{lp}\left(s_{int}(t) \cdot p^*(t)\right) + n(t) \\ &= \tilde{s}_{\text{tar}}(t) + \tilde{s}_{\text{int}}(t) + n(t) \end{aligned} \quad (6)$$

where $s(t)$ represents the measured signal, $n(t)$ denotes the noise and measurement errors, $\tilde{s}_{\text{int}}(t) = \mathcal{F}_{lp}\left(s_{\text{int}}(t) p^*(t)\right)$ is the signal resulting from the interference, and $\tilde{s}_{\text{tar}}(t) = \sum_{i=1}^{M'} a_i \exp(-j2\pi f_{b,i} t)$ is the beat signal of targets within the desired detection range. Equation (6) gives the general model of the FMCW radar measurements contaminated by strong interference.

### *C. Interference*

Radar systems face various types of interference due to the rapid increase in radio wireless applications. In particular, for FMCW radar systems, the related interference can be classified as the following four cases [22]–[24]: 1) FMCW

$$\begin{aligned} \tilde{s}(t) &= \mathcal{F}_{lp}\{[s_r(t) + s_{\text{int}}(t)] \cdot p^*(t)\} \\ &= \mathcal{F}_{lp}\left(s_{\text{int}}(t) \cdot p^*(t)\ \right) + \mathcal{F}_{lp}\left\{ \sum_{i=1}^{M} A_{tx} A_{rx,i} \exp\left[ -j2\pi \left( f_0\ t_i - \frac{Kt_i^2}{2} \right) \right] \cdot \exp(-j2\pi K t_i t) \right\} \\ &= \mathcal{F}_{lp}\left(s_{\text{int}}(t) \cdot p^*(t)\right) + \sum_{i=1}^{M'} \tilde{A}_{r,i} \exp\left[ -j2\pi \left( f_0 t_i - \frac{Kt_i^2}{2} \right) \right] \exp(-j2\pi K t_i t) \end{aligned} \quad (3)$$

interference with the same chirp rate; 2) FMCW interference with a different chirp rate; 3) CW interference; and 4) transient interference. These cases are illustrated in Fig. 2. In Case 1), the FMCW interference would result in a strong ghost target if it appears within the reception window of the system determined by the maximum detection range. In Cases 2) and 3), the FMCW and CW interference have a long time duration and lead to the nonconstant beat frequency after the dechirp processing. Due to the low-pass filtering, their occurrences are confined in a short time around the frequency intersecting moment. In Case 4), the spectrum of the transient (or pulse) interference with a rectangular amplitude in a short time can be considered as equidistant lines with a $\sin(x)/x$ envelope. Some of these frequency lines intersect with the reference FMCW signal of dechirp operation and then, as in Case 3), result in the short interference after low-pass filtering [23].

The above analysis indicates that the interference in Cases 2)–4) all cause contaminated measurements in certain time period within an FMCW sweep duration, which, in principle, can be tackled using the method described in this article (note that the interference with a very small sweep slope difference from that of the victim radar (i.e., extreme situations in case 2) could make all the signal samples contaminated, in which case the proposed approach and other zeroing plus reconstruction methods would not be applicable). Without loss of generality, we consider that the FMCW signal was contaminated by an FMCW interference with a different frequency slope, i.e., Case 2), in the following.

Assuming that an interfering FMCW radar is located at a distance $d_I$ away from the transceiver, the interference signal arriving at the receiving antenna can be expressed as

$$s_{\text{int}}(t) = A_I \exp\left[ j2\pi \left( f_{I,0}(t - t_I) + \frac{K_I}{2}(t - t_I)^2 \right) \right] \quad (7)$$

for $t_I < t < T_I + t_I$, where $A_I$ is the amplitude of the interference. $t_I = d_I/c$ is the time delay of the interference signal relative to the starting time of the transmission of the victim radar. $f_{I,0}$ is the starting frequency of the interference signal, and $K_I = B_I/T_I$ is the chirp rate of the interference signal with the bandwidth $B_I$ and the sweep duration $T_I$.

Then, the interference signal $\tilde{s}_{\text{int}}(t)$ obtained after dechirping and low-pass filtering can be explicitly expressed as

$$\tilde{s}_{\text{int}}(t) = \mathcal{F}_{lp}\left(s_{\text{int}}(t)\, p^*(t)\right) = \mathcal{F}_{lp}\{a_I \exp[j\Phi(t)]\} \quad (8)$$

where

$$\Phi(t) = 2\pi \left[ \left( \frac{K_I}{2} - \frac{K}{2} \right) t^2 + \left( f_{I,0} - f_0 - K_I t_I \right) t \right] \quad (9)$$

$$a_I = A_I A_{tx} \exp\left[ j2\pi \left( \frac{K_I}{2} t_I^2 - f_{I,0} t_I \right) \right]. \quad (10)$$

Taking the first derivative of the phase $\Phi(t)$ with respect to time, one can get the instantaneous beat frequency

$$f_{b,I}(t) = -\frac{1}{2\pi} \frac{\partial \Phi_I(t)}{\partial t} = (K_1 t + K_2) \quad (11)$$

where $K_1 = (K - K_I)$ and $K_2 = (f_0 - f_{I,0} + K_I t_I)$ are constant coefficients. According to (11), the beat frequencies resulting from the interference are time-varying. After the low-pass filtering in (8), its frequency bandwidth and the time of occurrence are confined, but the time-varying property is not affected. By contrast, the beat frequencies of targets are constant, as shown in (6). This difference between the beat frequencies of targets and interferer makes that the interference mitigation can be done in either the time or $t$–$f$ domain [14].

## III. Matrix-Pencil Method-Based Interference Mitigation

A model-based interference mitigation approach for the FMCW radar system is presented in this section. This approach can operate in either the time domain or the $t$–$f$ domain. Without loss of generality, its details are illustrated through the time-domain processing for the interference mitigation in the following.

### A. Discrete Signal in the Time Domain

From (6), the discrete signal measurements can be written as

$$\begin{aligned} s[k] &= \tilde{s}_{\text{tar}}[k] + \tilde{s}_{\text{int}}[k] + n[k] \\ &= \sum_{i=1}^{M'} a_i z_i^k + \tilde{s}_{\text{int}}[k] + n[k] \end{aligned} \quad (12)$$

where $z_i = \exp(j2\pi f_{b,i} \Delta t)$, $\Delta t$ is the sampling interval, and $k = 0, 1, \ldots, N-1$ is the sampling indices of the $N$ time-domain samples in an FMCW sweep. As analyzed above, the interference component $\tilde{s}_{\text{int}}$ appears in a short period in a sweep; thus, only some of the measured signal samples, e.g., from $N_1$ to $N_2$, are contaminated, where $0 \le N_1 < N_2 \le N-1$. Since the desired targets' signal $\tilde{s}_{\text{tar}}$ is a sum of exponential components, it is natural to suppress the interference by cutting out the contaminated samples from the measurements and then reconstructing the cutout samples with the uncontaminated measurements and the model of the desired signal. As the clipped sample reconstruction is generally converted to an estimation problem of exponential components, it can be implemented with root-MUltiple SIgnal Classification (root-MUSIC), Prony's method [25], and so on. To more efficiently and accurately reconstruct the cutout samples, we suggest using MP method in this article, which leads to the proposed MP method-based interference mitigation.

### B. Interference Mitigation

The flowchart of the MP method-based interference mitigation for FMCW radars is shown in Fig. 3. The detailed processing involves two main steps.

*1) Interference Detection and Cutting Out:* Based on the analysis in Sections II-B and II-C, the beat frequencies of targets are generally constant in a sweep, while the interference after dechirping and low-pass filtering still exhibits nonstationary spectral property within its duration. Taking advantage of this spectral difference, the interference and its duration can be detected with many approaches, such as energy spikers' detection [26], constant false alarm rate (CFAR) thresholding [27], complex baseband oversampling [28], or other methods in

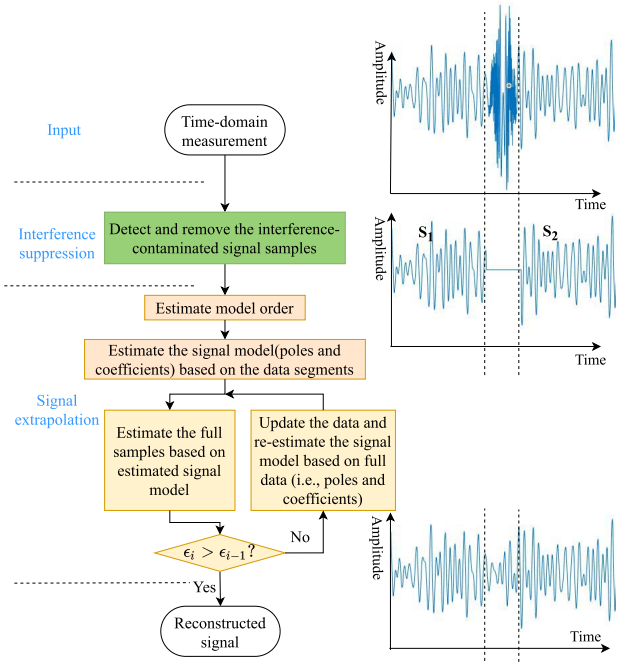


Fig. 3. Flowchart of the proposed MP-based interference mitigation approach.

the time or $t$–$f$ domain. After determining the location of the interference, the contaminated signal samples can be completely removed for interference suppression. However, it also eliminates part of the energy of the desired signals, which would cause SNR degradation of the resultant range profiles.

*2) Signal Extrapolation:* To overcome the SNR degradation of the targets' signals caused by the interference suppression, the removed signal samples can be reconstructed by using the interference-free samples and the corresponding signal model $\tilde{s}_{\text{tar}}$. Generally, the all-pole signal model $\tilde{s}_{\text{tar}}[k]$ is unknown and has to be estimated from the interference-free samples. In this article, the MP method is applied to estimate the model parameters (i.e., model order, signal poles, and coefficients) by simultaneously accounting for the interference-free samples in front of and behind the clipped ones. Moreover, to alleviate the impact of the noise and signal discontinuity of the interference-free samples on the estimation of the signal model of targets, an iterative fusion process is introduced to minimize the estimation error of the signals on both sides of the clipped region relative to the interference-free measurements. If the estimation error fulfills the desired requirement after a few iterations, the signals in the cutout region are reconstructed.

### C. Signal Fusion and Reconstruction

After cutting out the interference-contaminated samples indexed from $N_1$ to $N_2$, the interference-free measurements in (12) can be represented as

$$s[k] = \sum_{i=1}^{M'} a_i z_i^k + n[k] \tag{13}$$

where $k = 0, 1, \ldots, N_1 - 1, N_2 + 1, N_2 + 2, \ldots, N - 1$. Therefore, a gap is formed between the two signal sample segments from 0 to $N_1 - 1$ and from $N_2 + 1$ to $N$, as illustrated in the second plot on the right-hand side of Fig. 3. As the useful signals in this gap are also eliminated due to the interference clipping, it would cause some SNR loss of the final coherent processing results (e.g., range profile and R-D map). To overcome this problem, in the next step, we try to reconstruct the useful signals in the gap based on the signal model (13) and the interference-free measurements on the both sides.

As mentioned in Section I, here, the signal reconstruction can be converted to a signal fusion problem. We suggest using the MP-based fusion method in [18] and [19] to implement the signal reconstruction, but no incoherence correction between different signal segments is needed.

For the convenience of description, we denote the signals before and after the clipped region as $s_1$ and $s_2$, given by

$$\begin{cases} s_1[k] = s[k], & k = 0, 1, \ldots, N_1 - 1 \\ s_2[k] = s[k + N_2 + 1], & k = 0, 1, \ldots, N - N_2 - 2. \end{cases} \tag{14}$$

Then, the detailed steps of the signal reconstruction are presented as follows.

First, estimate the all-pole signal model (13) with the MP method based on the front and back signal segments, i.e., $s_1$ and $s_2$.

Generally, the signal model order $M'$ is estimated according to the Akaike information criterion (AIC), the Bayesian information criterion (BIC), the subspace-based automatic model order selection (SAMOS) [29], [30], and so on. As SAMOS is considered to be one of the most general and robust approaches to model order selection and outperforms the aforementioned methods based on the information theoretic criterion, it is used in this article. The signal poles can be estimated with the MP method. Different from the signal pole estimation with continuous uniform signal samples, the Hankel matrices based on the discontinuous signals $s_1$ and $s_2$ are constructed in a slightly different way [18], [19]. First, two Hankel matrices are constructed as

$$\begin{aligned} \mathbf{H}_{i0} &= \left[\mathbf{D}_0^i, \mathbf{D}_1^i, \ldots, \mathbf{D}_{L-1}^i\right] \\ \mathbf{H}_{i1} &= \left[\mathbf{D}_1^i, \mathbf{D}_2^i, \ldots, \mathbf{D}_L^i\right] \end{aligned} \tag{15}$$

with

$$\mathbf{D}_k^i = [s_i[k], s_i[k+1], \ldots, s_i[M_i - L - 1 + k]]^T, \quad i = 1, 2 \tag{16}$$

where $^T$ denotes the transpose operation, and $M_1 = N_1$ and $M_2 = N - N_2 - 1$ are the lengths of $s_1$ and $s_2$, respectively. $L$ is the MP parameter, and $\hat{M}' < L < \min(M_1 - \hat{M}', M_2 - \hat{M}')$, where $\hat{M}'$ is the estimated signal model order (without explicit statement, the $\hat{}$ notation represents the estimated value of a corresponding parameter).

The Hankel matrices constructed above can be vertically stacked as

$$\mathbf{X}_0 = \begin{bmatrix} \mathbf{H}_{10} \\ \mathbf{H}_{20} \end{bmatrix}, \quad \mathbf{X}_1 = \begin{bmatrix} \mathbf{H}_{11} \\ \mathbf{H}_{21} \end{bmatrix}. \tag{17}$$

Then, the matrix pencil $\mathbf{L}(\lambda) = \mathbf{X}_1 - \lambda \mathbf{X}_0$ can be evaluated to get the estimates the signal poles $z_i$ in (13) [18], [19]. To get

the eigenvalues of this matrix pencil, we take advantage of the singular value decomposition (SVD)-based method in [16]. Taking the SVD of the matrix $\mathbf{X}_0$ and $\mathbf{X}_1$, we get

$$\mathbf{X}_0 = \left[\mathbf{U}_0, \mathbf{U}_0'\right]\begin{bmatrix} \Sigma_{0,\hat{M}'} & 0 \\ 0 & \Sigma_{0,L-\hat{M}'} \end{bmatrix}\left[\mathbf{V}_0, \mathbf{V}_0'\right]^H \tag{18}$$

$$\mathbf{X}_1 = \left[\mathbf{U}_1, \mathbf{U}_1'\right]\begin{bmatrix} \Sigma_{1,\hat{M}'} & 0 \\ 0 & \Sigma_{1,L-\hat{M}'} \end{bmatrix}\left[\mathbf{V}_1, \mathbf{V}_1'\right]^H \tag{19}$$

where $^H$ denotes the conjugate transpose of a matrix, and $\Sigma_{0,\hat{M}'}$ and $\Sigma_{1,\hat{M}'}$ are the diagonal matrices containing $\hat{M}'$ dominant singular values of $\mathbf{X}_0$ and $\mathbf{X}_1$, respectively. The columns of $\mathbf{U}_0$, $\mathbf{U}_1$, $\mathbf{V}_0$, and $\mathbf{V}_1$ are the left and right singular vectors related to the dominant singular values. $(\mathbf{U}_0, \Sigma_{0,\hat{M}'}, \mathbf{V}_0)$ and $(\mathbf{U}_1, \Sigma_{1,\hat{M}'}, \mathbf{V}_1)$ are the singular value systems related to the signal subspace in $\mathbf{X}_0$ and $\mathbf{X}_1$, respectively. The rest terms in (18) and (19) form the corresponding singular value systems related to the so-called noise subspace.

To suppress the impact of the noise on the signal pole estimation, $\mathbf{X}_0$ and $\mathbf{X}_1$ can be approximated by their truncated SVD as $\mathbf{X}_{0T}$ and $\mathbf{X}_{1T}$

$$\mathbf{X}_0 \approx \mathbf{X}_{0T} = \mathbf{U}_0 \Sigma_{0,\hat{M}'} \mathbf{V}_0^H \tag{20}$$

$$\mathbf{X}_1 \approx \mathbf{X}_{1T} = \mathbf{U}_1 \Sigma_{1,\hat{M}'} \mathbf{V}_1^H. \tag{21}$$

Then, the signal poles $z_i$ can be estimated by solving the generalized eigenvalue problem $\det(\mathbf{L}(\lambda)) = 0$ of the matrix pair $\{\mathbf{X}_0; \mathbf{X}_1\}$, which is equivalent to the ordinary eigenvalue problem

$$\det\left(\Sigma_{0,\hat{M}'}^{-1} \mathbf{U}_0^H \mathbf{U}_1 \Sigma_{1,\hat{M}'} \mathbf{V}_1^H \mathbf{V}_0 - \lambda \mathbf{I}\right) = 0. \tag{22}$$

The signal pole estimations $\hat{z}_i = \lambda_i,\ i = 1, 2, \ldots, \hat{M}'$ are obtained.

After that, using the estimated signal model order $\hat{M}'$ and the signal poles $\hat{z}_i$, the complex amplitude $a_i$ can be cast as the least-squares problem $\mathbf{m} = \mathbf{Z}\mathbf{a}$, where $\mathbf{m} = [s_1, s_2]^T$ is the measured interference-free data, $\mathbf{Z}$ is the matrix formed by signal poles, and $\mathbf{a} = [a_1, a_2, \ldots, a_{\hat{M}'}]$ is the vector of the coefficients. Explicitly, it is represented as

$$\begin{bmatrix} s_1[0] \\ s_1[1] \\ \vdots \\ s_1[M_1-1] \\ s_2[0] \\ \vdots \\ s_2[M_2-1] \end{bmatrix} = \begin{bmatrix} 1 & 1 & \cdots & 1 \\ z_1 & z_2 & \cdots & z_{\hat{M}'} \\ \vdots & \vdots & \ddots & \vdots \\ z_1^{N_1-1} & z_2^{N_1-1} & \cdots & z_{\hat{M}'}^{N_1-1} \\ z_1^{N_2} & z_2 N_2 & \cdots & z_{\hat{M}'}^{N_2} \\ \vdots & \vdots & \ddots & \vdots \\ z_1^{N-1} & z_1^{N-1} & \cdots & z_1 N - 1 \end{bmatrix} \begin{bmatrix} a_1 \\ a_2 \\ \vdots \\ a_{\hat{M}'} \end{bmatrix}. \tag{23}$$

Second, after inserting the estimated signal poles $\hat{z}_i$ and the coefficients $\hat{a}_i$ into (13), the full beat signal in the sweep can be estimated by

$$\hat{s}[k] = \sum_{i=1}^{\hat{M}'} \hat{a}_i \hat{z}_i^k, \quad k = 0, 1, \ldots, N-1. \tag{24}$$

The estimated full beat signal indicates

$$\begin{cases} \hat{s}_1[k] = \hat{s}[k], & k \in [0, N_1 - 1] \\ \hat{s}_g[k - N_1] = \hat{s}[k], & k \in [N_1, N_2] \\ \hat{s}_2[k - N_2 - 1] = \hat{s}[k], & k \in [N_2 + 1, N - 1]. \end{cases} \tag{25}$$

Third, to improve the estimation of the full beat signal, we replace the $\hat{s}_1$ and $\hat{s}_2$ parts in $\hat{s}$ with the measurements $s_1$ and $s_2$. Then, the reconstructed full beat signal can be modified as

$$\hat{s}[k] = \begin{cases} s_1[k], & k \in [0, N_1 - 1] \\ \hat{s}_g[k - N_1], & k \in [N_1, N_2] \\ s_2[k - N_2 - 1], & k \in [N_2 + 1, N - 1]. \end{cases} \tag{26}$$

Next, the reconstructed signal $\hat{s}$ in (26) are used as a set of contiguous samples to reestimate the signal poles $z_i$ and the coefficients $a_i$ in (13) by using the traditional MP method [16].

Fourth, repeat steps (2) and (3) to update the reconstructed results. After the step (2) in each iteration, the $l^2$-norm of the differences between the estimated signals and their measured counterparts is examined to quantify the signal estimation accuracy

$$\epsilon_i = \left\| \hat{s}_1^{(i)} - s_1 \right\|_2^2 + \left\| \hat{s}_2^{(i)} - s_2 \right\|_2^2 \tag{27}$$

where $\hat{s}_1^{(i)}$ and $\hat{s}_2^{(i)}$ are the estimated counterparts of the measurements $s_1$ and $s_2$ in the $i$th iteration. If the signal difference in the $i$th iteration satisfies the requirement

$$\epsilon_i > \epsilon_{i-1} \tag{28}$$

then iteration will stop. Otherwise, it continues to improve the estimated model parameters. As $\epsilon_i$ is lower bounded by 0, it means that one could always get a convergent solution by gradually minimizing it.

After several iteration cycles, we get the most accurate recovery of the full beat signal. Finally, by taking corresponding operations on the reconstructed full beat signal, the range profile and Doppler information of targets can be obtained with substantially improved dynamic range and suppressed "noise" floor.

## IV. Numerical Simulations

To analyze the performance of the proposed MP-based method to interference mitigation, several sensing scenarios have been simulated. Its results are also compared with the traditional zeroing and three of the state-of-the-art methods, i.e., the Burg-based approach [11], the IVM-based method [12], and the IMAT method [13].

### A. Evaluation Metric

To facilitate quantitative evaluation of the accuracy of the reconstructed beat signals by different methods, we introduce two evaluation metrics: the relative signal-to-noise ratio (RSNR) and the correlation coefficient $\rho$. The RSNR and the correlation coefficient are defined as

$$\mathrm{RSNR}(\mathbf{s}_0, \hat{\mathbf{s}}) = 20 \log_{10} \frac{\|\mathbf{s}_0\|_2}{\|\mathbf{s}_0 - \hat{\mathbf{s}}\|_2} \tag{29}$$

$$\rho_{\mathbf{s}_0,\hat{\mathbf{s}}} = \frac{\hat{\mathbf{s}}^H \mathbf{s}_0}{\|\mathbf{s}_0\|_2 \cdot \|\hat{\mathbf{s}}\|_2} \tag{30}$$

TABLE I

PARAMETERS USED FOR SIMULATIONS FOR POINT-LIKE AND DISTRIBUTED TARGET SCENARIOS

| Parameter | Value | Unit |
|---|---|---|
| Center frequency | 3 | GHz |
| Bandwidth | 40 | MHz |
| FMCW sweep duration | 500 | $\mu s$ |
| Sweep slope | $8 \times 10^{10}$ | Hz/s |
| Transmit Power | 1 | Watt |
| Sampling frequency | 12 | MHz |
| Maximum unambiguous range | 8 | km |
| Number of samples in a sweep | 5360 | N/A |
| **Point target scenario** | | |
| Distances of three targets | 2, 5, and 5.1 | km |
| Interference duration | 10-50% | N/A |
| **Extended targets scenario** | | |
| Number of point targets | 15 | N/A |
| Distance between adjacent targets | $1 < d < 1.8$ | m |
| Interference duration relative to the sweep duration | 24.3% | N/A |

where $\mathbf{s}_0$ is the vector of a clean reference beat signal (without interferences and noise) and $\hat{\mathbf{s}}$ is the beat signal formed by the measured interference-free samples and the reconstructed signal samples in the cutout region. $\|\cdot\|_2$ denotes the $\ell^2$-norm operator. If the signal samples in the cutout region are reconstructed with sufficient accuracy, an RSNR larger than the SNR of the input signal can be obtained according to (29). Thus, the larger the obtained RSNR is, the more accurate the recovered signal samples are.

The correlation coefficient is commonly used to evaluate the similarity of two signals. Its formulation in (30) is a normalized inner product between the reconstructed signal and the reference one, which specifically represents the rotation angle between the two signals. The correlation coefficient satisfies $0 \leq |\rho_{\mathbf{s}_0,\hat{\mathbf{s}}}| \leq 1$. If $|\rho_{\mathbf{s}_0,\hat{\mathbf{s}}}| = 1$, then the reconstructed signal $\hat{\mathbf{s}}$ is a linear function of the reference signal $\mathbf{s}_0$ with a phase difference of $\angle\rho_{\mathbf{s}_0,\hat{\mathbf{s}}}$ (i.e., argument of $\rho_{\mathbf{s}_0,\hat{\mathbf{s}}}$). That is to say, a correlation coefficient with a larger modulus and a smaller argument indicates a better recovery performance.

### *B. Point Target Scenario*

First, we demonstrate the performance of the proposed MP-based interference mitigation approach in the point target scenario. The parameters of the FMCW radar system used for the simulation are shown in Table I. Three point targets are placed at a distance of 2, 5, and 5.1 km, respectively, away from the transceiver. The amplitudes of the scattered signals from the three targets from the near to further distances are set to be 1, 0.2, and 0.1, respectively.

The victim FMCW radar system suffers from strong interference from an aggressor FMCW radar with the same operational center frequency but an opposite sweep slope and a time advancement of 75 $\mu$s relative to the starting time of the victim sweep. After dechirping, the interference-contaminated beat signal is acquired and illustrated in Fig. 4(a). The strong interference appears at the interval from 165 to 265 $\mu$s (indicated by the red solid-line rectangle), which still exhibits

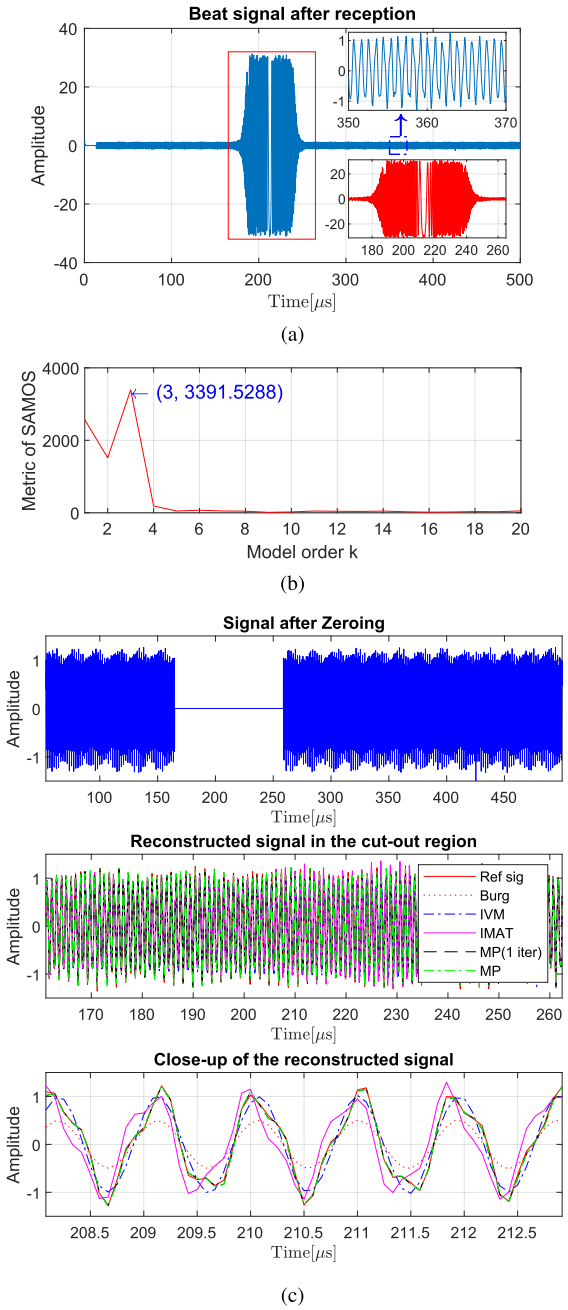


Fig. 4. Numerical simulation for interference mitigation in the point target scenario. (a) Interference-contaminated beat signal. (b) Metric values of SAMOS for model order estimation. (c) Results after interference mitigation.

as a chirp-like signal [see the bottom-right inset in Fig. 4(a)]. Meanwhile, for clarity, part of the interference-free beat signal (from 350 to 370 $\mu$s indicated by the blue dashed-dotted rectangle) is zoomed in and shown in the top-right inset. It is clear that the beat signal of targets is composed of the sinusoidal components. Moreover, the white Gaussian noise with the SNR of 15 dB is added to the signal to account for the thermal noise and measurement errors of the radar system.

The interference-contaminated beat signal produces a range profile with significantly increased noise floor (see "sig_Int" in Fig. 5(a) where the two targets at the further distances are

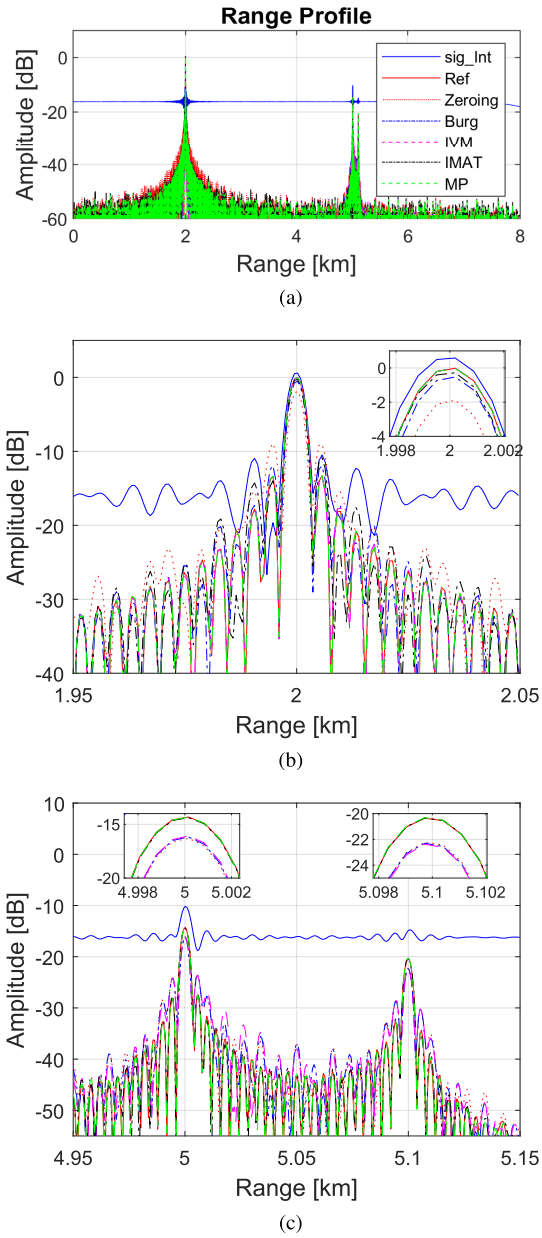


Fig. 5. (a) Range profiles of the targets obtained with the interference-contaminated signal, the interference-free reference signal, and the signals processed with zeroing, the Burg-based method, IVM, IMAT, and the MP-based method. (b) and (c) Close-ups of the range profile around the distances of targets, respectively.

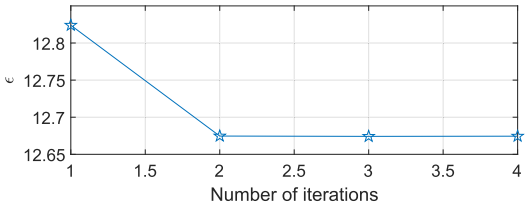


Fig. 6. Convergence of the difference between the estimated signal and their measured counterpart with the iterations of the MP-based approach.

almost shadowed by the raised noise floor) if the range compression is performed directly by using the FFT. To mitigate the interference by using the proposed MP-based approach,

TABLE II
RESULTS OF QUANTITATIVE EVALUATION OF THE RECOVERED SIGNALS IN THE POINT TARGET SCENARIO

| | | RSNR [dB] | $\rho$ |
|---|---|---|---|
| Burg-based method | | 14.9524 | $0.9845\exp(j0.0002)$ |
| IVM | | 19.5652 | $0.9945\exp(j0.005)$ |
| IMAT | | 13.1957 | $0.9790\exp(-j0.0799)$ |
| MP-based approach | $1^{st}$ iteration | 28.6502 | $0.9992\exp(-j0.0001)$ |
| | Converged | 28.6602 | $0.9992\exp(j0.0001)$ |

the interference-contaminated samples of the signal are first detected and cut out (i.e., zeroing with a rectangular window [15]). Zeroing the interference-contaminated samples results in two separate signal segments with a gap in-between [see the top figure in Fig. 4(c)], which causes not only power loss of targets' signals but also high sidelobes of the range profile, thus degrading the performance of target detection. To overcome these effects, the proposed MP-based interference mitigation method is used to reconstruct the signal samples in the cutout gap based on the signal model (24) and the rest interference-free ones in front and back. Before reconstruction, the model order was estimated to be three by using the SAMOS method [see Fig. 4(b)], which agrees with the true value. Then, by exploiting the proposed iterative scheme, the signal samples in the gap were recovered with sufficient accuracy, as shown in the middle plot and a close-up of them in the bottom figure in Fig. 4(c).

For comparison, the recovered signals with the Burg-based method, IVM, and IMAT, as well as the interference-free reference signal (with the noise), are shown in the middle and bottom figures. For the Burg-based method and IVM, the same model order as that of the MP-based method was used. For the IMAT, the parameters of the adaptive threshold were computed using the equations with $m = 2.5$ (a parameter used by IMAT in [13]; without explicit statement, we will use $m$ to refer to the same parameter in the following) for the empirically best performance. One can see that the signal recovered with the proposed MP-based method has the best agreement with the reference one. Meanwhile, the IVM method achieves more accurate reconstruction of the signals in the cutout region than the Burg-based method and IMAT in this case. These observations are also confirmed through the quantitative evaluation in Table II. Both the bottom plot in Fig. 4(c) and $\rho$ in Table II show that the IMAT recovered the samples in the cutout region with a large phase difference compared to the other three model-based methods.

To further examine the accuracy of the reconstructed signals, the range profiles of targets are constructed by taking the FFT of them and shown in Fig. 5. For comparison, the range profiles obtained with the interference-contaminated and interference-free reference beat signals [i.e.,"sig_Int" and "Ref" in Fig. 5(a), respectively] are also presented. Note all the range profiles are normalized by the maximum of the range profile acquired with the interference-contaminated signal.

According to Fig. 5(a), all the interference mitigation methods, i.e., zeroing, the Burg-based method, IVM, IMAT, and the

MP-based method, significantly reduce the "noise" floor of the range profile and, thus, increase its dynamic range compared to the one obtained with the interference-contaminated signal. Among them, the zeroing method is computationally most efficient by simply replacing the interference-contaminated samples with zeros, however resulting in a gap between the front and rear signal samples. Consequently, it causes high sidelobes and some SNR loss in the range profile compared to that obtained with the reference signal. Specifically, from the insets in Fig. 5(b) and (c), the peaks of targets' range profiles obtained after zeroing are 1.9 dB lower than those formed with the reference signal and the signal reconstructed with the MP-based method. Although the Burg- and IVM-based methods efficiently interpolate the samples in the cutout gap and result in comparable/identical range profiles as the reference signal for the target at the short distance, they fail to overcome the power loss for the two weak targets at the further distances and get range profiles close to that of the zeroing method [see the insets in Fig. 5(c)]. The IMAT overcomes the power loss for all targets but the large phase difference of its reconstructed samples from the reference results in asymmetrical sidelobes of the range profile [see Fig. 5(b)]. By contrast, the MP-based method not only conquers the power loss of the range profile for all the targets but also accurately reconstructs their range profiles in terms of both the mainlobe and the sidelobes. Therefore, its recovered signal samples in the cutout region are more accurate than those obtained by the Burg-based method, IVM, and IMAT.

In addition, compared to the straightforward extrapolation of the Burg-based method and IVM, the proposed MP-based approach introduces a heuristic iterative scheme to refine the sample reconstruction. To demonstrate the effect of the MP method and the iterative scheme, the recovered signal by the MP-based approach in the first iteration is shown in Fig. 4(c), and the convergence of difference $\epsilon$ with respect to the number of iterations is displayed in Fig. 6. These reveal that the MP-based method gets sufficiently accurate reconstruction of the samples in the cutout region in the first iteration ["MP(1 iter)" in Fig. 4(c)] compared to the other methods, and then, the iterative scheme further improves the recovered samples.

### *C. Extended Target Scenario*

The applicability of the proposed method to extended target scenarios is investigated in this section. The parameters used for the simulation are shown in Table I. An extended target was constructed with 15 point scatterers randomly generated with adjacent interdistances between 1 and 1.8 m (i.e., less than the range resolution of 3.75 m in the simulation setup). The target was located at the range of 3–3.025 km away from the transceiver. The amplitudes and phases of the scattered signals from these closely spaced scatterers were random values with uniform distribution in $[0, 0.05]$ and uniform distribution in $[0, 2\pi]$, respectively. A beat signal with the SNR of 15 dB was synthesized by adding white Gaussian noise to consider measurement errors and thermal noise of the system and also contaminated by a strong interference with the same center frequency but a sweep slope of $-0.98$ times that of the victim radar. The resultant beat signal is illustrated in Fig. 7(a).

To mitigate interference, the interference-contaminated samples are first detected and cut out. The result is shown in top figure in Fig. 7(d). Then, the signal model order was estimated by using the SAMOS method based on the other interference-free samples. However, due to the strong correlation among the beat signals scattered by the closely spaced scatterers, the model order was selected to be two by using the SAMOS method, which is significantly different from the theoretical value of 15 [see Fig. 7(b)]. Thus, the SAMOS method cannot work properly in such scenarios. To investigate the reason for the failure of the SAMOS, we checked the singular value distribution of the matrix used for model order selection, as shown in Fig. 7(c). Based on Fig. 7(c), it is obvious that a proper model order should be not smaller than four. Taking the model order of four, the signal samples in the cutout region were recovered by using the Burg-, IVM- and MP-based methods; these samples were also reconstructed by using the IMAT with $m = 3$. The obtained signals are shown in the two bottom plots in Fig. 7(d) and (e), respectively. It is clear that the IVM-based interpolation is not stable, and a blow-up is observed in Fig. 7(e). Meanwhile, compared to the Burg-based method and IMAT, the proposed MP-based method reconstructed the signal samples with the best agreement with the reference signal [see the bottom plot in Fig. 7(d)]. Taking the FFT of the signal obtained after zeroing and the recovered signals with the Burg-based method, IMAT, and the MP-based method, the related range profiles of targets were constructed and shown in Fig. 8(a). As expected, the range profile of the targets constructed with the signal recovered with the MP-based method has the best agreement with that formed using the reference signal.

Moreover, we also reconstructed the signal samples in the cutout region using the three methods by setting the model order to be 15. Again, a blow-up as in Fig. 7(e) is observed in the recovered signal by the IVM-based method (here the figure is omitted for conciseness). Thus, it indicates that the instability of the IVM-based method may not be caused by the underestimation of the signal model order. Meanwhile, the recovered signal by the Burg-based method is still less accurate than that obtained with the MP-based method [see Figs. 7(f) and 8(b)]. The RSNRs and correlation coefficients of the recovered signals by the Burg-based method, IMAT, and MP-based approach are quantitatively evaluated and shown in Table III. It is clear that the MP-based method recovered the signal with the highest RSNRs and correlation coefficients with largest magnitudes and smallest phases (except when model order $= 4$), which further confirms that the MP-based method is superior to the Burg-based method and IMAT in terms of the signal reconstruction accuracy.

Finally, we want to mention that, when multiple point targets in the same range bin are very close to each other, the Burg-based method could occasionally outperform the proposed MP-based method (for conciseness, we do not show it here). As the close targets in a range bin result in highly correlated beat frequencies, the characteristic polynomial of the corresponding AR model has many closely spaced roots.

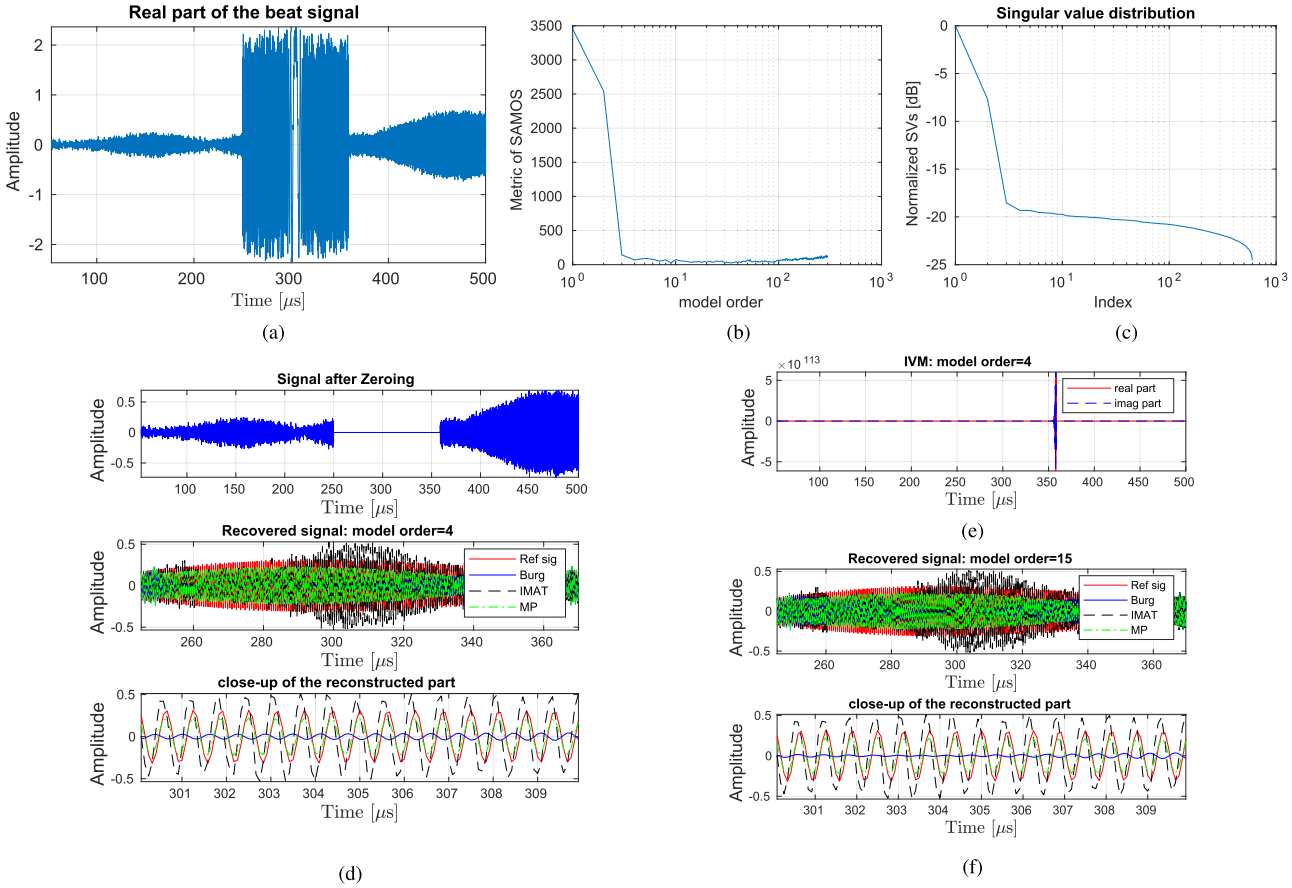


Fig. 7. Numerical simulation for interference mitigation in the extended target scenario. (a) Interference-contaminated beat signal of an extended target. (b) Metric values of the SAMOS approach for model order selection. (c) Singular values distribution of the matrix constructed for model order selection. (d) Results after interference mitigation: top: beat signal after zeroing; middle: reference beat signal and the beat signals recovered with the Burg- and MP-based methods with the model order of four; and bottom: close-up view of the recovered samples in the cutout region. (e) Beat signal recovered by the IVM with the model order of four. (f) Recovered beat signals with the model order of 15.

TABLE III

RSNRs AND CORRELATION COEFFICIENTS OF THE RECOVERED SIGNALS WITH THE BURG-BASED METHOD, IMAT, AND THE MP-BASED APPROACH

| | RSNR[dB] | | $\rho$ | |
|---|---|---|---|---|
| | Model order=4 | Model order=15 | Model order=4 | Model order=15 |
| Burg | 6.5348 | 7.7070 | $0.8832\exp(j0.0216)$ | $0.912\exp(j0.03)$ |
| MP | 12.7255 | 12.7055 | $0.9734\exp(-j0.0252)$ | $0.9732\exp(-j0.0259)$ |
| IMAT | 6.3175 | | $0.9002\exp(-j0.1687)$ | |

The proposed MP-based method tends to estimate some dominant sinusoidal components (i.e., roots) that are close to the real roots in the mean square error sense, while the Burg-based method attempts to estimate the coefficients of the characteristic polynomial of the AR model. Apparently, the latter operation is easier in such cases; thus, the Burg-based method could result in more accurate signal estimation.

### *D. Effect of the Model Order Underestimation*

Besides the comparison of the recovered signals with different model orders in Section IV-C, the effect of model order underestimation on the performance of the reconstructed signal was further investigated through Monte Carlo simulation using the parameters for the point target scenario. Simulations were run 100 times with different noise implementations at each case of the cutout gap size, which is, for generality, defined by the ratio between the number of the removed interference-contaminated samples and the number of all signal samples in a sweep. The average RSNRs and $\rho$'s of recovered signals are shown in Fig. 9. Note the IMAT reconstructs the samples in the cutout region based on a threshold (with $m = 2.5$) but does not need model order estimation. Due to the instability of IVM, its results are not presented. One can see that the results of both the Burg-based method and MP-based approach only slightly degrade when an underestimated model order of two was used compared to that with the exact model order of three. Meanwhile, although the IMAT performs better than the Burg-based method in terms of RSNR when the gap size is not larger than 30%, its recovered

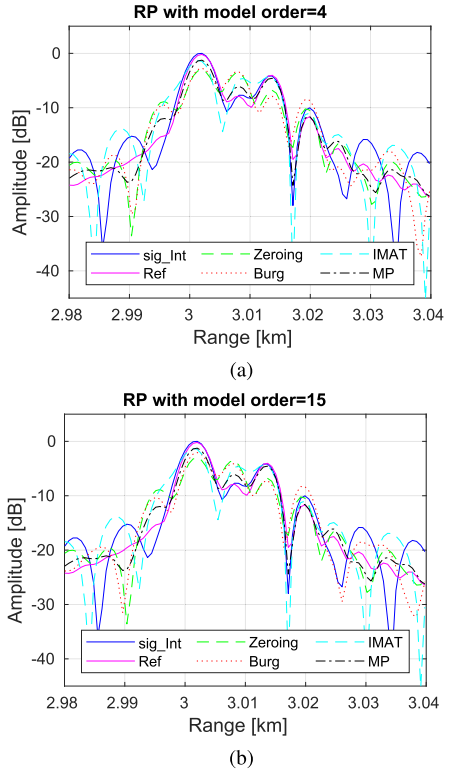


Fig. 8. Range profile of the extended target obtained with the reference signal, the interference-contaminated beat signal, the signals obtained with zeroing, and the signals recovered by the Burg- and MP-based methods with (a) model order of four and (b) model order of 15.

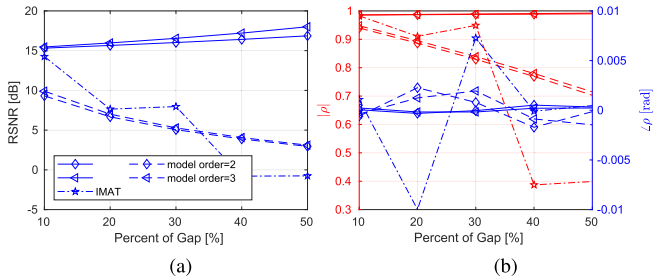


Fig. 9. Impact of model order estimation on the performance of the sample reconstruction. (a) and (b) RSNRs and correlation coefficients of the recovered signals with the model order of two (indicated by ◇) and model order of three (◁) by the Burg-based method (dashed line) and the MP-based approach (solid line). The results obtained with the IMAT method are indicated by the dashed-dotted line.

signals have a large phase difference from that of the reference [see Fig. 9(b)]. At the same time, the IMAT is always inferior to the MP-based method according to both RSNRs and $\rho$'s of the recovered signals.

On the other hand, note that an underestimated model order could, in principle, cause some degradation of the accuracy of the recovered samples with the MP-based method. However, this degradation could depend on the correlation among the exponential components [17], [31]. As each singular value spectrum is not attributed to a single exponential component, an underestimated model order would lead to a certain loss of the power of some exponential components but does not mean that they would not be recovered entirely, especially for the case with highly correlated complex exponents [see Fig. 7(d) and (f)].

### *E. Effect of the Length of Interferences and SNR*

The impact of the interference duration (equivalently, the size of the cutout gap caused by interference suppression) and the SNR on the performance of the proposed MP-based method for signal recovery is investigated in this section. The simulation parameters for the point target scenario in section IV-B were used here. In the simulation, the SNR changes from $-30$ to 10 dB with steps of 10 dB, and at each SNR, the interference duration increases from 10% to 50% with steps of 10%. To investigate the statistical performance of the proposed MP-based approach, 100 Monte Carlo runs were conducted at each SNR with each specific gap size. The average RSNRs and $\rho$'s of the recovered signals with the Burg-based method, IMAT, and the MP-based method are shown in Fig. 10 (due to the blow-ups of signals recovered with the IVM-based method, its related results are omitted here).

From Fig. 10(a), one can see that the RSNRs of the signals reconstructed with the Burg- and MP-based methods are almost identical when SNR $< 0$ dB, and they gradually improve and become larger than the SNRs with the increase in the size of the cutout region. This is because, when SNR $< 0$ dB, the zeroing operation eliminates, besides interferences, more noise power than that of useful signals. Then, the RSNRs of the reconstructed signals would improve compared to the original SNRs as long as the useful signal samples in the cutout region can be recovered with certain accuracy by using either of the model-based methods (i.e., the Burg- and MP-based methods). When SNR $\geq 0$ dB, the zeroing operation suppresses more signal power than noise power in the cutout region. The MP-based method accurately recovers the signal samples in the cutout gap by jointly using the sampling at both sides of the gap; thus, the RSNRs of obtained signals are improved in contrast to the original SNRs. In particular, when the cutout gap occupies 50% of the whole sweep, almost half of the noise power is suppressed; thus, 3-dB improvement of RSNR relative to the SNR of the input signal can be obtained as long as the useful signal samples in the cutout region are accurately reconstructed [see Fig. 10(a)]. On the other hand, the Burg-based method separately forward/backward extrapolates signal samples in the gap based on the data on one side of the gap but fails to recover the signal samples in the gap with sufficient accuracy, which leads to decreased RSNRs of the reconstructed signals compared to the original SNRs. Therefore, in terms of the RSNR of the recovered signal, the Burg- and MP-based methods obtain comparable results when SNR $< 0$ dB, while the latter one outperforms the former one when SNR $\geq 0$ dB. Furthermore, based on Fig. 10(a), the RSNR of the recovered signals by the IMAT seems almost constantly inferior to those by the Burg- and MP-based methods at all the SNRs with gap sizes from 10% to 50%.

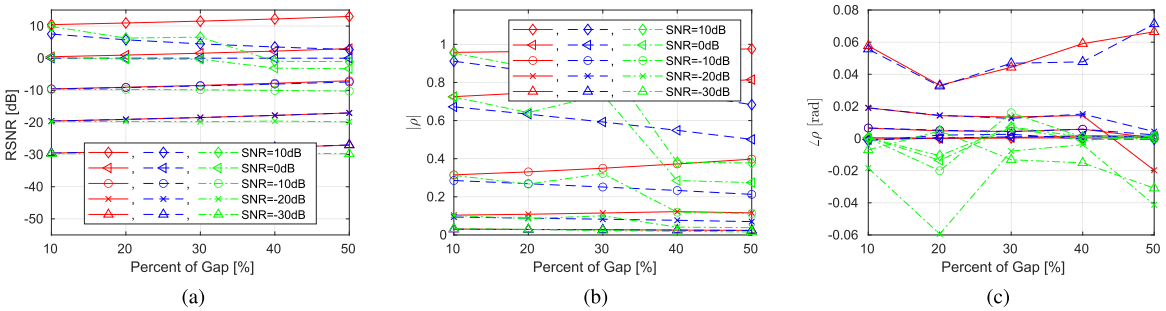


Fig. 10. Impact of gap duration and SNR on the accuracy of the reconstructed signals with the Burg-based method (dashed blue lines), IMAT (dash-dotted green lines), and MP (solid red lines)-based methods. (a) RSNRs with different gap durations. (b) and (c) Moduli and phases of the correlation coefficients with respect to different gap durations.

Regarding the modulus of the correlation coefficient (i.e., $|\rho|$), Fig. 10(b) shows that the MP-based method constantly obtains comparable/better signal reconstruction compared to the Burg-based method and IMAT. Moreover, with the increase in the SNR and the interference duration, the performance advantage of the MP-based method to the Burg-based one and IMAT becomes larger. However, the phases of the correlation coefficients (i.e., $\angle\rho$) between the recovered signals with both MP- and Burg-based methods and the reference are comparable when the interference duration is smaller than 40% [see Fig. 10(c)]. They gradually reduce to zero with the increase in the SNR of the original signal. However, compared to those of both MP- and Burg-based methods, the phases of the correlation coefficients of the signals obtained by the IMAT show much greater fluctuations with different gap sizes. Therefore, according to the above analyses, the MP-based method generally achieves more accurate signal reconstruction than the Burg-based method and IMAT in terms of both RSNR and the correlation coefficient of the recovered signal.

### *F. Computational Efficiency*

The Burg-based method, IVM, and IMAT are all very computational efficient as the first two methods just separately extrapolate the data in the gap from both sides, while the third one utilizes the efficient FFT. By contrast, the proposed MP-based method uses the SVD and an iterative scheme to recover the samples in the cutout region by jointly taking advantage of the data from both sides. Thus, its computational load is slightly heavier than that of the Burg- and IVM-based methods, which depends on the number of iterations in practice. For a scenario with moderate interference duration (20%–30%) and SNR, the MP-based method generally needs several iterations. Specifically, for the simulation in Section IV-B, it took 0.02, 0.15, 0.03, and 27.05 s for the Burg-based method, IVM, IMAT, and MP-based method, respectively, when they were implemented in MATLAB and run on a computer with Intel Core i5-3470 central unit processor (CPU) @ 3.2 GHz and 8-GB random access memory (RAM). In this case, four iterations were performed in the MP-based method. To accelerate the MP-based method, the Lanczos iteration [32] or the randomized algorithm [33] for the SVD could be exploited in the future.

## V. Experimental Results

In this section, experimental results with radar observations of an industrial chimney and raindrops are presented to demonstrate the effectiveness and accuracy of the proposed MP-based interference mitigation method.

### *A. Experimental Setups*

The experiments used the TU Delft PARSAX S-band (3.1315 GHz) full-polarimetric FMCW radar system [34]. In the experiments, we consider the interference problem encountered when all components of the full-polarimetric scattering matrix are measured simultaneously. To this end, PARSAX radar transmits simultaneously two orthogonally polarized (e.g., H- and V-pol) and mutually orthogonal in time FMCW chirps (e.g., up-chirp for H-pol and down-chirp for V-pol) through two transmission channels and then simultaneously receives H- and V-pol scattered signals through the four receiver channels (i.e., HH-, HV-, VH-, and VV-pol channels, where the two capital letters represent, respectively, the polarizations of the transmitter and the receiver in order). In the V-pol signal path in the receiver, the V-pol scattered signals (i.e., a mixture of HV- and VV-pol signals) pass through the HV- and VV-polarimetric receiver channels. The HV- and VV-pol signals are separated through deramping with the transmitted up- and down-chirps, respectively, and low-pass filters. In such an operational mode, the interference between HV- and VV-pol scattered signals exists at the time moment when instantaneous frequencies of the up- and down-chirps are coming closer to each other so that the resulting beat signals are within the bandwidth of the low-pass filter in the receiver. This kind of interference is categorized as Case 2 in Fig. 2. A similar interference exists between the HH- and VH-pol scattered signals. As the co-pol (i.e., HH and VV) signals are generally much stronger than the cross-pol (i.e., VH and HV) ones, this interference has a larger effect on the cross-polarized signals. Therefore, the cross-polarized (specifically, HV-pol) signals are processed for the following demonstration.

In Experiment 1, we used an industrial chimney as a stationary target and took measurements for a single sweep. The chimney is about 1.07 km away from PARSAX radar

(a) (b)

Fig. 11. Experimental measurement setup. (a) PARSAX radar on the roof of the EEMCS Faculty Building. (b) Industrial chimney used as a stationary target.

TABLE IV
RADAR PARAMETERS FOR THE TWO EXPERIMENTAL MEASUREMENTS

| **Parameter** | **Value** |
|---|---|
| Center frequency | 3.1315 GHz |
| Bandwidth | 40 MHz |
| Time duration of a sweep | 1 ms |
| Number of samples per sweep | 16384 |
| Maximum range | 18.75 km |
| Number of sweeps per CPI | 512 |
| Waveforms for simultaneous full-pol measurement | Up-chirp for H-pol channel; Down-chirp for V-pol channel. |

(see Fig. 11). In Experiment 2, PARSAX radar pointed vertically observes a rain storm, which can be considered as a distributed target. The parameters for experimental measurements are listed in Table IV.

### *B. Experiment 1: Stationary Isolated Target (Chimney)*

The acquired HV-pol beat signal (i.e., "sig_Int" in the solid red line) scattered from the chimney is shown in Fig. 12(a). It was contaminated by the strong VV-pol signal arrived together at the receiving antenna, and the interference-contaminated samples are indicated by a dashed red rectangle in Fig. 12(a). For comparison, the reference HV-pol signal (i.e., "ref sig") acquired by only transmitting a single H-pol up-chirp signal is also presented.

To suppress the VV-pol interference, the received signal was processed by using the zeroing, the Burg-based method, IVM, IMAT, and the proposed MP-based interference mitigation method. For the Burg-based method, IVM, and the MP-based method, SAMOS was initially used to estimate the signal model order, and a model order of two was selected, which is highly underestimated considering the complex environment surrounding the chimney. Hence, we decided to select the model order empirically based on the normalized singular value distribution of the matrix used by SAMOS [see Fig. 12(b)]. With a threshold of $10^{-2}$ (i.e., 20 dB) for the normalized SVs, a model order of 40 was selected and used by the three methods for signal reconstruction. For the IMAT, the parameters are computed based on the equations in [13] with $m = 3$. The obtained signals by these methods are shown in Fig. 12(c) and (d). Comparing the signals in Fig. 12(c), the MP-based method almost accurately reconstructs the clipped samples in the interference-contaminated region, while the Burg-based method and IMAT recover these samples with underestimated/overestimated amplitudes in some regions. By contrast, the IVM-based method leads to a blow-up in the recovered beat signal [see Fig. 12(d)], which again shows its instability.

Moreover, the range profiles constructed with the interference-contaminated signal, reference signal, and the signals acquired after interference mitigation are displayed in Fig. 13(a) (due to invalid signal recovery of the IVM-based method, its RP is omitted). It is clear that the range profile obtained with the interference-contaminated signal has a higher "noise floor" in contrast to those formed with other signals, which would mask weak targets. For the convenience of comparison, the close-ups of the range profiles of the chimney at the distance of 1.07 km and some weak targets at the distance of 4.3 km in Fig. 13(a) are shown in Fig. 13(b) and (c). From Fig. 13(c), a clear peak for a weak target at the distance of 4.24 km can be observed in the range profiles generated with the reference signals and the signals recovered after interference mitigation. By contrast, a deep null is seen at the same position in the range profile formed with the interference-contaminated signal, which could be caused by the destructive interference between the interference and the target's signal. Moreover, the range profiles obtained with signals after mitigating the interference by using the Burg-based method, IMAT, and the MP-based method are comparable to the reference one and have lower sidelobes for the weak targets around the distance of 4.3 km. On the other hand, the range profile of the chimney acquired after processing with the proposed MP-based interference mitigation is almost identical to the one formed with the reference signal. However, the zeroing caused a void of signal samples, and the Burg-based method and IMAT underestimated the signal amplitude in the cutout region; thus, they cause higher sidelobes and power loss in the constructed range profiles [see the insets in Fig. 13(b)].

### *C. Experiment 2: Distributed Target (Rain)*

In this experiment, we used 512 sweeps as a coherent processing interval (CPI) for full-polarimetric measurements of rain droplets. After simple preprocessing to suppress the direct coupling, the acquired HV-pol signals in all the sweeps are shown in Fig. 14, where the interference-contaminated samples are located in the time interval from 0.4 to 0.6 ms. The interference was caused by the VV-pol signals, which are generally much stronger than the desired HV-pol signals (see the much larger amplitudes of the interference-contaminated samples relative to the rest). Thus, after the R-D processing, the formed R-D map of the rain droplets is completely overwhelmed by the interference, as shown in Fig. 16(a).

As the raindrops are moving targets, we suggest first taking the FFT with respect to the slow time in a CPI and then performing the interference mitigation to the time signal along each Doppler bin to avoid the possible detrimental impact of errors caused by interference mitigation on the Doppler information. Fig. 15(a) shows the time signal in a Doppler bin after taking the FFT along the slow time, and the interference is still observed in the interval from 0.4 to 0.6 ms. Applying the

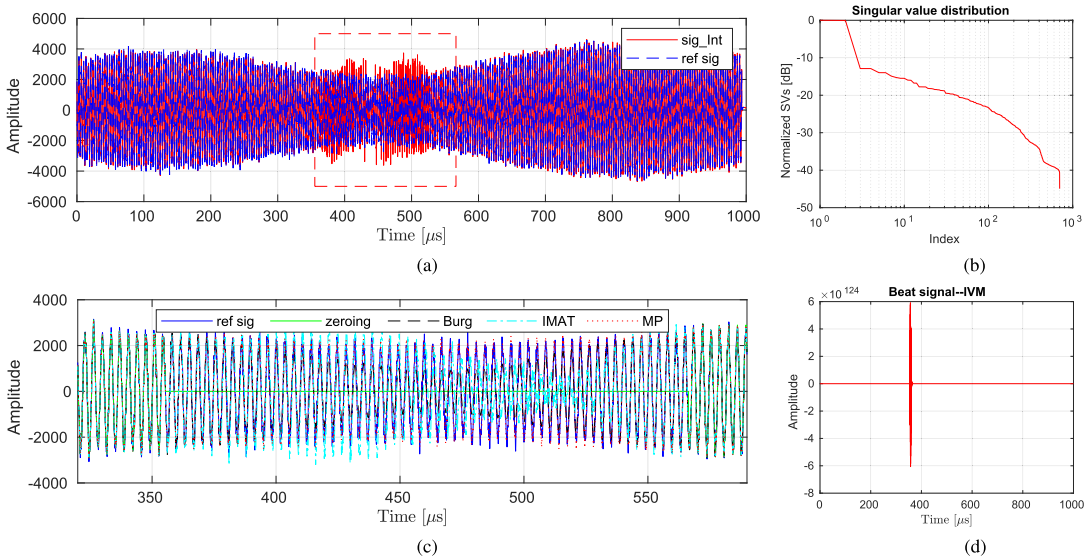


Fig. 12. Beat signal acquired in one FMCW sweep for the chimney observation. (a) Measured beat signals with (i.e., "sig_Int" in the red solid line) and without the cross-polarimetric interference (i.e., "ref sig" in the blue dashed line). (b) Signals around the interference-contaminated region after interference mitigation using zeroing, Burg- and MP-based methods. (c) Recovered beat signal with the IVM-based method.

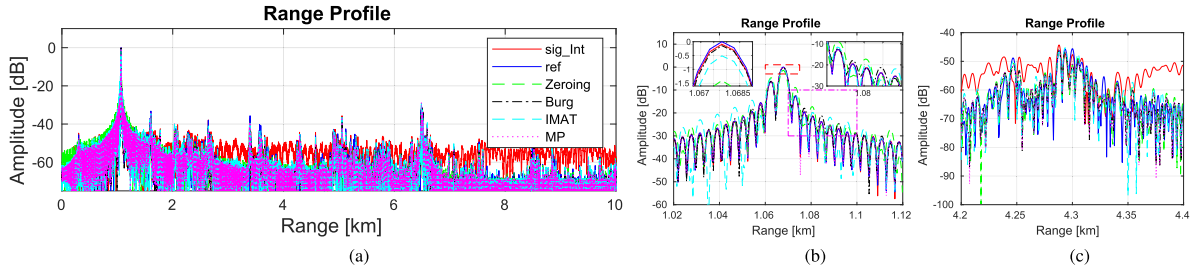


Fig. 13. Range profiles of the Chimney scenario obtained with the signals before and after interference mitigation. (a) Range profiles of the scenario within 10 km from the radar. (b) and (c) Zoomed-in views of the range profiles of the targets at the distances of 1.07 and 4.3 km from the radar, respectively.

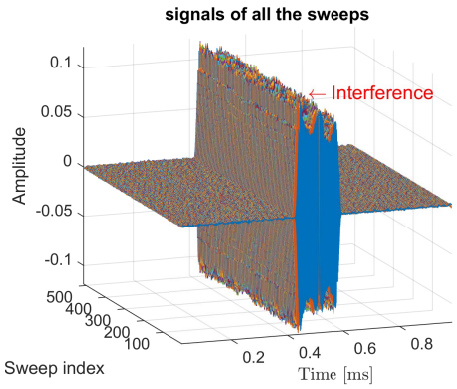


Fig. 14. Signals of all the sweeps scattered from rain droplets.

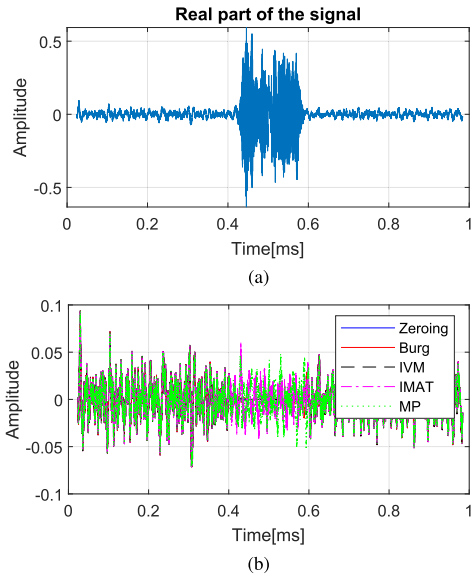


Fig. 15. Time signals at a Doppler bin after taking FFT along the slow-time dimension. (a) and (b) Time signal before and after interference mitigation.

proposed MP-based interference mitigation method, zeroing, the Burg-based method, IVM, and IMAT to this time signal, the resultant signals are presented in Fig. 15(b). The Burg- and IVM-based methods reconstruct only some samples that are close to the front and rear available measurements in the cutout gap with underestimated amplitudes, while both IMAT and the MP-based method manage to recover all the samples in the gap. However, as the reference signal is unavailable in this case, we could not directly evaluate the accuracy of their recovered samples; alternatively, the R-D map of rain droplets will be used in the following. Note that, for the rain

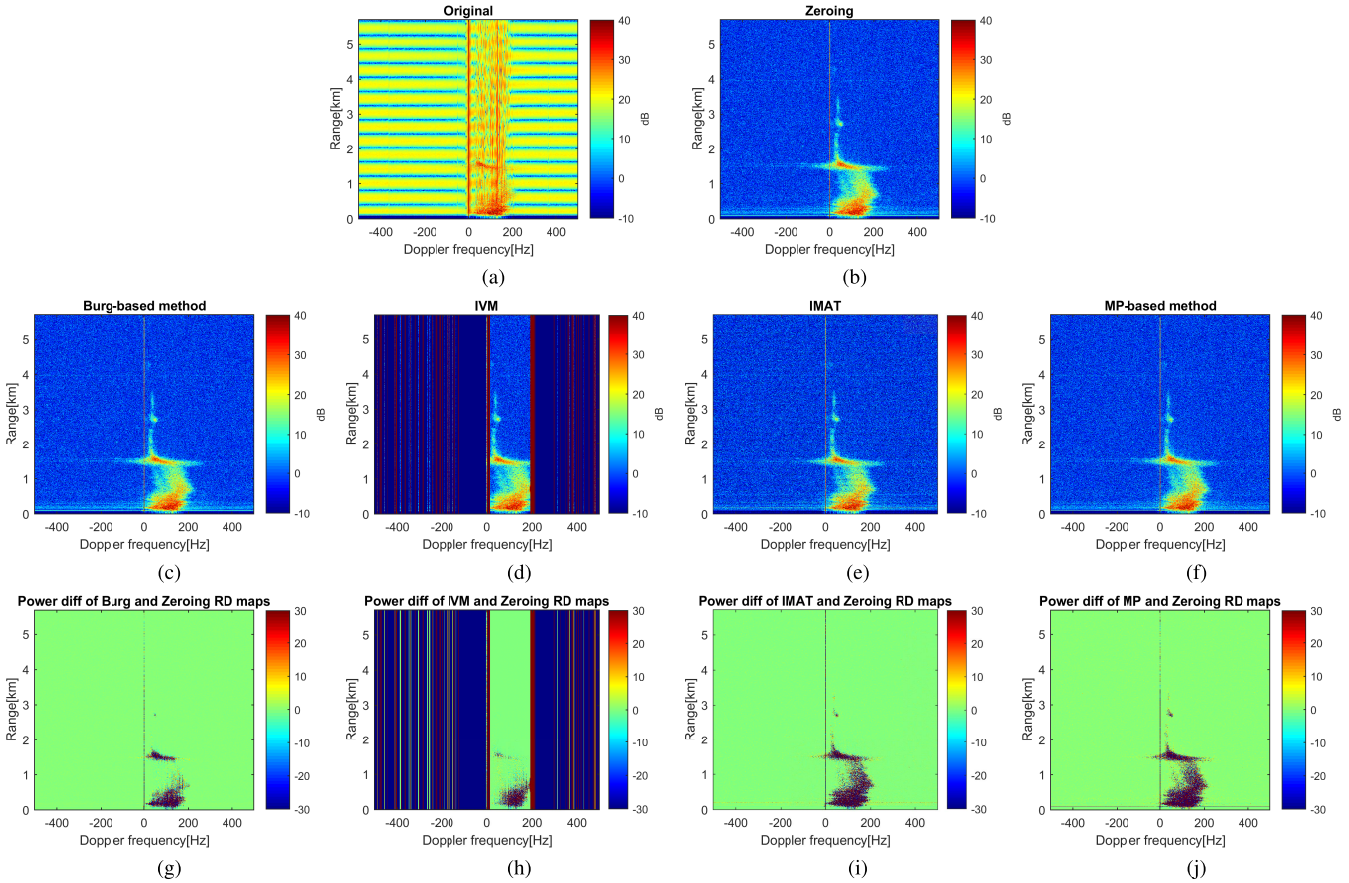


Fig. 16. R-D processing results of the rain data. (a) RD map obtained with the original interference-contaminated signals. (b)–(f) are formed by the signals after interference mitigation by using the zeroing, the Burg-based method, IVM, IMAT, and the MP-based method, respectively. (g)–(j) Corresponding power differences between the RD maps in (c)–(f) and (b).

dataset, the SAMOS method could not estimate proper model orders, either. Thus, we empirically determine the model order of the signal in each Doppler bin based on the normalized singular value distribution of the matrix used by SAMOS with a threshold of $10^{-4}$. The estimated signal model order was used by the Burg-, IVM- and MP-based methods to reconstruct the signal in the cutout region. Meanwhile, the IMAT was implemented with the parameter $m = 3$.

After mitigating the interferences for the time signals in all Doppler bins, an FFT is taken along the fast time to get the R-D map of the raindrops. Fig. 16(b)–(f) presents the obtained R-D maps in the logarithmic scale of the moduli of signals after interference mitigation with zeroing, the Burg-based method, IVM, IMAT, and the MP-based approach, respectively. It is clear that, due to the instability of the IVM-based method, it could not reconstruct a proper R-D map of the rain droplets [see Fig. 16(d)]. By contrast, the other four R-D maps [see Fig. 16(b), (c), (e), and (f)] are visually almost identical, and their qualities are noticeably improved compared to that obtained without interference mitigation [see Fig. 16(a)].

Due to the lack of ground truth reference, we alternatively assess the improvement of the R-D maps obtained with the Burg-based method, IVM, IMAT, and the MP-based method relative to the one got with zeroing by computing the power differences between the pixels of the R-D maps of the three signal reconstruction methods and the zeroing method. The results are shown in the linear scale in Fig. 16(g)–(j). One can see that the power difference between the R-D maps of MP-based method and zeroing in Fig. 16(j), compared with that in Fig. 16(g), presents a pattern much closer to the R-D maps in Fig. 16(b), (c), (e), and (f). As, in the rain dataset, the strong VV-pol interferences appear at a similar time interval in all the sweeps within the CPI, the zeroing method eliminates the signal samples within this time interval (i.e., between about 0.4 and 0.6 ms) in all the sweeps. Thus, the power difference of the R-D maps of zeroing and the other three methods are determined by the contribution of the beat signal samples in the cutout region. Theoretically, the beat signals of rain droplets in the cutout time interval in a CPI can be considered as the acquired data by using an FMCW radar with narrower bandwidth (i.e., shorter FMCW sweep duration) but keep other system parameters unchanged; thus, they can form a similar R-D map as that obtained with the full-sweep signals in the CPI but with lower range resolution. Namely, the more accurate the signal samples recovered by the Burg-based method, IVM, and the MP-based method in the cutout region are, the closer to the actual R-D map the pattern of the power difference between the R-D maps of these methods and the zeroing approach. Therefore, the MP-based method gets a more accurate estimation of the signals in

the cutout region than the Burg-based method. Meanwhile, compared to Fig. 16(i), Fig. 16(j) has a closer pattern to the R-D maps in Fig. 16(b), (c), (e), and (f) (see the area around the range of 2.8 m and the Doppler frequency of 50 Hz, and the region around the range of 1 km and the Doppler frequency of 100 Hz). Thus, the samples recovered by the MP-based method are more accurate than those by the Burg-based method, IVM, and IMAT.

## VI. Conclusion

In this article, we present an MP-based interference mitigation method for FMCW radar systems. The proposed method exploits the feature of the desired beat signals as a sum of exponential sinusoidal components, which is different from the chirp-like waveforms of interferences after dechirping on reception, for interference suppression. The method is implemented in two steps by first detecting and cutting out the interference-contaminated samples and then recovering the signal samples in the cutout region based on the exponential sinusoidal model of desired beat signals. It addresses the discontinuity of the signals caused by the traditional zeroing technique and overcomes the power loss of useful signals. Meanwhile, it results in lower sidelobes of the range profile of a target. Moreover, providing an accurate, compared to the existing methods (i.e., the Burg-based method, IVM, and IMAT), reconstruction of the signal after direct implementation, it significantly improves the accuracy of the reconstructed signals in the cutout region by an iterative estimation scheme, which has demonstrated through both numerical simulations and experimental results. The numerical simulations also reveal that the proposed method can robustly work in scenarios with a low SNR (down to 0 dB) and with a long interference duration (up to 50% of a sweep). In addition, the proposed MP-based method can be extended to 2-D or high-dimensional cases to mitigate interferences directly in a higher dimensional space (e.g., RD or range-DOA domains), especially for point-target scenarios, which would be considered in future work.

## Acknowledgment

The authors acknowledge the contribution of N. Cancrinus to this research by testing the applicability of the matrix-pencil method to the beat signal reconstruction.

## References

[1] J.-G. Kim, S.-H. Sim, S. Cheon, and S. Hong, "24 GHz circularly polarized Doppler radar with a single antenna," in *Proc. Eur. Microw. Conf.*, Oct. 2005, p. 4.

[2] J. Bechter, C. Sippel, and C. Waldschmidt, "Bats-inspired frequency hopping for mitigation of interference between automotive radars," in *IEEE MTT-S Int. Microw. Symp. Dig.*, May 2016, pp. 1–6.

[3] Y. Kim, "Identification of FMCW radar in mutual interference environments using frequency ramp modulation," in *Proc. 10th Eur. Conf. Antennas Propag. (EuCAP)*, Apr. 2016, pp. 1–3.

[4] C. Aydogdu, M. F. Keskin, N. Garcia, H. Wymeersch, and D. W. Bliss, "RadChat: Spectrum sharing for automotive radar interference mitigation," *IEEE Trans. Intell. Transp. Syst.*, vol. 22, no. 1, pp. 416–429, Jan. 2021.

[5] J. Khoury, R. Ramanathan, D. McCloskey, R. Smith, and T. Campbell, "RadarMAC: Mitigating radar interference in self-driving cars," in *Proc. 13th Annu. IEEE Int. Conf. Sens., Commun., Netw. (SECON)*, Jun. 2016, pp. 1–9.

[6] J.-H. Choi, H.-B. Lee, J.-W. Choi, and S.-C. Kim, "Mutual interference suppression using clipping and weighted-envelope normalization for automotive FMCW radar systems," *IEICE Trans. Commun.*, vol. E99.B, no. 1, pp. 280–287, 2016.

[7] F. Jin and S. Cao, "Automotive radar interference mitigation using adaptive noise canceller," *IEEE Trans. Veh. Technol.*, vol. 68, no. 4, pp. 3747–3754, Apr. 2019.

[8] F. Uysal, "Synchronous and asynchronous radar interference mitigation," *IEEE Access*, vol. 7, pp. 5846–5852, 2019.

[9] J. Ren, T. Zhang, J. Li, L. H. Nguyen, and P. Stoica, "RFI mitigation for UWB radar via hyperparameter-free sparse SPICE methods," *IEEE Trans. Geosci. Remote Sens.*, vol. 57, no. 6, pp. 3105–3118, Jun. 2019.

[10] B.-E. Tullsson, "Topics in FMCW radar disturbance suppression," in *Proc. Radar Syst. (RADAR)*, 1997, pp. 1–5.

[11] S. Neemat, O. Krasnov, and A. Yarovoy, "An interference mitigation technique for FMCW radar using beat-frequencies interpolation in the STFT domain," *IEEE Trans. Microw. Theory Techn.*, vol. 67, no. 3, pp. 1207–1220, Mar. 2019.

[12] M. Toth, P. Meissner, A. Melzer, and K. Witrisal, "Performance comparison of mutual automotive radar interference mitigation algorithms," in *Proc. IEEE Radar Conf. (RadarConf)*, Apr. 2019, pp. 1–6.

[13] J. Bechter, F. Roos, M. Rahman, and C. Waldschmidt, "Automotive radar interference mitigation using a sparse sampling approach," in *Proc. Eur. Radar Conf. (EURAD)*, Oct. 2017, pp. 90–93.

[14] G. Babur, "Processing of dual-orthogonal CW polarimetric radar signals," Ph.D. dissertation, Dept. Telecommun., Delft Univ. Technol., Delft, The Netherlands, 2009.

[15] G. Babur, Z. Wang, O. A. Krasnov, and L. P. Ligthart, "Design and implementation of cross-channel interference suppression for polarimetric LFM-CW radar," *Proc. SPIE*, vol. 7745, Sep. 2010, Art. no. 774520.

[16] T. K. Sarkar and O. Pereira, "Using the matrix pencil method to estimate the parameters of a sum of complex exponentials," *IEEE Antennas Propag. Mag.*, vol. 37, no. 1, pp. 48–55, Feb. 1995.

[17] Y. Hua and T. K. Sarkar, "Matrix pencil method for estimating parameters of exponentially damped/undamped sinusoids in noise," *IEEE Trans. Acoust., Speech, Signal Process.*, vol. 38, no. 5, pp. 814–824, May 1990.

[18] Y. Q. Zou, X. Z. Gao, X. Li, and Y. X. Liu, "A matrix pencil algorithm based multiband iterative fusion imaging method," *Sci. Rep.*, vol. 6, no. 1, May 2016, Art. no. 19440.

[19] J. Wang, P. Aubry, and A. Yarovoy, "Wavenumber-domain multiband signal fusion with matrix-pencil approach for high-resolution imaging," *IEEE Trans. Geosci. Remote Sens.*, vol. 56, no. 7, pp. 4037–4049, Jul. 2018.

[20] Y. Hua, "Estimating two-dimensional frequencies by matrix enhancement and matrix pencil," *IEEE Trans. Signal Process.*, vol. 40, no. 9, pp. 2267–2280, Sep. 1992.

[21] F.-J. Chen, C. C. Fung, C.-W. Kok, and S. Kwong, "Estimation of two-dimensional frequencies using modified matrix pencil method," *IEEE Trans. Signal Process.*, vol. 55, no. 2, pp. 718–724, Jan. 2007.

[22] G. M. Brooker, "Mutual interference of millimeter-wave radar systems," *IEEE Trans. Electromagn. Compat.*, vol. 49, no. 1, pp. 170–181, Feb. 2007.

[23] M. Goppelt, H.-L. Blöcher, and W. Menzel, "Automotive radar—Investigation of mutual interference mechanisms," *Adv. Radio Sci.*, vol. 8, pp. 55–60, Sep. 2010.

[24] T. Schipper, M. Harter, T. Mahler, O. Kern, and T. Zwick, "Discussion of the operating range of frequency modulated radars in the presence of interference," *Int. J. Microw. Wireless Technol.*, vol. 6, nos. 3–4, pp. 371–378, Jun. 2014.

[25] M. H. Hayes, *Statistical Digital Signal Processing and Modeling*. New York, NY, USA: Wiley, 1996, pp. 129–198.

[26] M. Kunert, "The eu project mosarim: A general overview of project objectives and conducted work," in *Proc. 9th Eur. Radar Conf.*, Oct. 2012, pp. 1–5.

[27] C. Fischer, H. L. Blocher, J. Dickmann, and W. Menzel, "Robust detection and mitigation of mutual interference in automotive radar," in *Proc. 16th Int. Radar Symp. (IRS)*, Jun. 2015, pp. 143–148.

[28] S. Murali, K. Subburaj, B. Ginsburg, and K. Ramasubramanian, "Interference detection in FMCW radar using a complex baseband oversampled receiver," in *Proc. IEEE Radar Conf. (RadarConf)*, Apr. 2018, pp. 1567–1572.

[29] J.-M. Papy, L. De Lathauwer, and S. Van Huffel, "A shift invariance-based order-selection technique for exponential data modelling," *IEEE Signal Process. Lett.*, vol. 14, no. 7, pp. 473–476, Jul. 2007.
[30] Y. Sun, T. Fei, and N. Pohl, "Two-dimensional subspace-based model order selection methods for FMCW automotive radar systems," in *Proc. Asia–Pacific Microw. Conf. (APMC)*, Nov. 2018, pp. 1247–1249.
[31] J. E. F. del Rio and T. K. Sarkar, "Comparison between the matrix pencil method and the Fourier transform technique for high-resolution spectral estimation," *Digit. Signal Process.*, vol. 6, no. 2, pp. 108–125, Apr. 1996.
[32] G. Golub and C. Van Loan, "Matrix computations," in *Johns Hopkins Studies in the Mathematical Sciences*. Baltimore, MD, USA: Johns Hopkins Univ. Press, 2013.
[33] H. Li, G. C. Linderman, A. Szlam, K. P. Stanton, Y. Kluger, and M. Tygert, "Algorithm 971: An implementation of a randomized algorithm for principal component analysis," *ACM Trans. Math. Softw.*, vol. 43, no. 3, pp. 1–14, Jan. 2017.
[34] O. A. Krasnov, L. P. Ligthart, . Li, P. Lys, and F. van der Zwan, "The PARSAX—Full polarimetric FMCW radar with dual-orthogonal signals," in *Proc. Eur. Radar Conf.*, Oct. 2008, pp. 84–87.

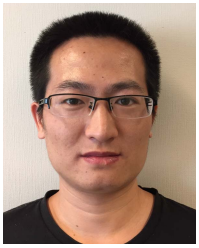

**Jianping Wang** (Member, IEEE) received the B.Sc. degree from the North China University of Technology, Beijing, China, in 2009, the M.Sc. degree from the Beijing Institute of Technology, Beijing, in 2012, and the Ph.D. degree from the Delft University of Technology, Delft, The Netherlands, in 2018, all in electrical engineering.

From August 2012 to April 2013, he worked as a Research Associate at the University of New South Wales (UNSW), Sydney, NSW, Australia, on frequency-modulated continuous-wave (FMCW) synthetic aperture radar (SAR) signal processing for formation flying satellites. He is currently a Post-Doctoral Researcher with the Group of Microwave Sensing, Signals and Systems (MS3), Delft University of Technology. His research interests include microwave imaging, signal processing, and antenna array design.

Dr. Wang was a TPC Member of the IET International Radar Conference, Nanjing, China, in 2018. He was a finalist of the Best Student Paper Awards in the International Workshop on Advanced Ground Penetrating Radar (IWAGPR), Edinburgh, U.K., in 2017, and the International Conference on Radar, Brisbane, QLD, Australia, in 2018. He has served as a Reviewer of IEEE TRANSACTIONS ON GEOSCIENCE AND REMOTE SENSING (TGRS), IEEE GEOSCIENCE AND REMOTE SENSING (GRS) LETTERS, IEEE SENSORS JOURNAL, IEEE TRANSACTIONS ON IMAGE PROCESSING (TIP), *Journal of Applied Geophysics*, and so on.

**Min Ding** received the B.S. degree in electrical engineering from North China Electric Power University, Baoding, China, in 2017, and the M.S. degree in telecommunications and sensing systems from the Delft University of Technology, Delft, The Netherlands, in 2019.

She is currently with State Grid Corporation of China, Beijing, China. Her research interests include radar signal processing and frequency-modulated continuous-wave (FMCW) radar interference mitigation.

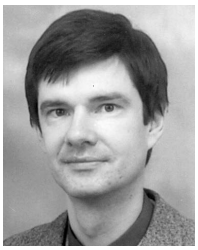

**Alexander Yarovoy** (Fellow, IEEE) received the Diploma degree (Hons.) in radiophysics and electronics and the Candidate Phys. & Math. Sci. and Doctor Phys. & Math. Sci. degrees in radiophysics from Kharkiv State University, Kharkiv, Ukraine, in 1984, 1987, and 1994, respectively.

In 1987, he joined the Department of Radiophysics, Kharkiv State University, as a Researcher, where he became a Professor in 1997. From September 1994 to 1996, he was with the Technical University of Ilmenau, Ilmenau, Germany, as a Visiting Researcher. Since 1999, he has been with the Delft University of Technology, Delft, The Netherlands, where he has been leading as the Chair of Microwave Sensing, Signals and Systems since 2009. He has authored or coauthored more than 250 scientific or technical articles, four patents, and 14 book chapters. His main research interests are in ultrawideband microwave technology and its applications (particularly radars) and applied electromagnetics (particularly ultra-wideband (UWB) antennas).

Prof. Yarovoy was a recipient of the European Microwave Week Radar Award for the paper that best advances the state of the art in radar technology in 2001 (together with L. P. Ligthart and P. van Genderen) and 2012 (together with T. Savelyev). In 2010, together with D. Caratelli, he got the Best Paper Award of the Applied Computational Electromagnetic Society (ACES). He has served as the Chair and the TPC Chair of the 5th European Radar Conference (EuRAD' 08), Amsterdam, The Netherlands, and the Secretary of the 1st European Radar Conference (EuRAD 04), Amsterdam. He has served as the Co-Chair and the TPC Chair of the Xth International Conference on Ground Penetrating Radar (GPR 2004) in Delft. Since 2008, he has served as the Director of the European Microwave Association. He has served as a Guest Editor of five special issues of the IEEE TRANSACTIONS and other journals. Since 2011, he has been an Associate Editor of the *International Journal of Microwave and Wireless Technologies*.